COMPASS: AN UPPER LIMIT ON COSMIC MICROWAVE BACKGROUND POLARIZATION AT AN ANGULAR SCALE OF 20'

PHILIP C. FARESE,[1,2] GIORGIO DALL'OGLIO,[3] JOSHUA O. GUNDERSEN,[4] BRIAN G. KEATING,[5] SLADE KLAWIKOWSKI,[6] LLOYD KNOX,[7] ALAN LEVY,[8] PHILIP M. LUBIN,[8] CHRIS W. O'DELL,[9] ALAN PEEL,[7] LUCIO PICCIRILLO,[10] JOHN RUHL,[1,11] AND PETER T. TIMBIE[6]

ABSTRACT

COMPASS is an on-axis 2.6 m telescope coupled to a correlation polarimeter operating at a wavelength of 1 cm. The entire instrument was built specifically for cosmic microwave background (CMB) polarization studies. We report here on observations of 2001 February–April using this system. We set an upper limit on E-mode polarized anisotropies of 1036 μK^2 (95% confidence limit) in the l range 93–555.

Subject headings: cosmic microwave background — cosmology: observations — instrumentation: polarimeters

On-line material: color figures

1. INTRODUCTION

The recent detection of acoustic peaks in the cosmic microwave background (CMB) temperature power spectrum supports the scenario that we live in a critical density universe consisting mainly of dark matter and dark energy. In this model, large-scale structures grew via gravitational instability from seeds laid down by quantum fluctuations in a period of inflation in the early universe (Hu & Dodelson 2002). Concordance models, in which the anisotropy measurements are combined with observations of the large-scale structure in the universe and observations of distant supernovae, sharpen this picture even further.

Further clues from the early universe have recently been found in the polarization of the CMB. The polarization signal is typically divided into two types: E modes, which arise from scalar (density) perturbations in the early universe, and B modes, which are caused by tensor (gravitational wave) perturbations and by gravitational lensing. The first attempts to measure CMB polarization occurred shortly after the discovery of the CMB almost 40 years ago. With the detection of the acoustic peaks in the temperature power spectrum now fully in hand, a variety of experiments have focused on polarization measurements. The DASI experiment has recently detected

the E-mode signal at angular scales of $1°–0°2$ (Kovac et al. 2002) at a level of $\sim$5 μK. DASI also detected the temperature-polarization (TE) cross-correlation signal. Both detections are consistent with predictions from ΛCDM models. Because the small-scale polarization signal is expected to arise from the same processes that produced the acoustic peaks in the temperature anisotropy, detection of this signal has provided reassuring confirmation of the temperature measurements and further support for the inflationary scenario. *WMAP* has detected the TE polarization signal on angular scales greater than $0°2$ (Kogut et al. 2003). On scales below $5°$ the signal is consistent with that expected from the observed temperature power spectrum. However, on large scales greater than $10°$, excess power is detected that is consistent with reionization occurring in the redshift range $11 < z_r < 30$ with an optical depth of $\tau = 0.17 \pm 0.04$. Further measurements of the polarization power spectrum will improve the determination of the fundamental cosmological parameters. In particular, measurement of the B-mode signal will constrain or detect primordial gravitational waves created during inflation.

We report here a 95% confidence upper limit at an angular scale of $\sim$0°3 in the frequency range 26–36 GHz from one season of observations with the Cosmic Microwave Polarization at Small Scales (COMPASS) telescope. Although this limit is about a factor of 6 above the level of the recent polarization detections at this scale, the measurements are important for understanding the effects of foreground emission. Foreground emission from Galactic and extragalactic sources can cause both E- and B-mode contamination near the level of sensitivity we have achieved. In our range of observing frequencies synchrotron radiation and emission from spinning dust are expected to be the dominant foregrounds. COMPASS observes near the north celestial pole (NCP). While the NCP is an exceptionally convenient region of the sky to observe from the Northern Hemisphere, it is not particularly clean of potential galactic foreground radiation. The absence of any detection of foreground signal in this region is encouraging for future measurements.

This paper is organized as follows. We describe the COMPASS instrument in § 2, the calibration in § 3, and the observations in § 4. In §§ 5, 6, 7, and 8 we explain the data selection and analysis procedures, and in § 9 we give the results.

[1] Department of Physics, University of California, Broida Hall, Building 572, Santa Barbara, CA 93106.

[2] Current address: Princeton University, Princeton, NJ 08544.

[3] Department of Physics "E. Amaldi," Universita Roma Tre, via Della Vasca Navale 84, Rome, Italy.

[4] Department of Physics, University of Miami, James L. Knight Physics Building, 1320 Campo Sano Drive, Coral Gables, FL 33146.

[5] Center for Astrophysics and Space Sciences, University of California, San Diego, 9500 Gilman Drive, La Jolla, CA 92093.

[6] Department of Physics, University of Wisconsin, 2531 Sterling Hall, Madison, WI 53706.

[7] Department of Physics, University of California, 1 Shields Avenue, Davis, CA 95616.

[8] Department of Physics, University of California, Broida Hall, Building 572, Santa Barbara, CA 93106.

[9] Christopher W. O'Dell Department of Atmospheric and Oceanic Sciences, University of Wisconsin, Madison, WI 53706.

[10] Department of Physics and Astronomy, University of Wales, P.O. Box 913, Cardiff CF24 3YB, UK.

[11] Current address: Case Western Reserve University, 10900 Euclid Avenue, Cleveland, OH 44106.

2. INSTRUMENT

COMPASS uses a receiver that was originally coupled to a corrugated feed horn with a $7°$ FWHM beam for a large angular scale CMB polarization experiment known as POLAR (Keating et al. 2003). In order to observe smaller angular scales where a larger primordial polarization signal is expected, a dielectric lens was added to the POLAR optical system and this horn+lens combination was coupled to a 2.6 m on-axis Cassegrain telescope to form COMPASS. Here we present an overview of the instrument; further instrumental details can be found in Farese et al. (2003) and Farese (2003).

2.1. Polarimeter

The COMPASS polarimeter implements state-of-the-art High-Electron Mobility Transistor (HEMT) amplifiers that operate in the 26–36 GHz frequency range (Ka band). These amplifiers are maintained at ≈ 20 K and provide coherent amplification with a gain of ≈ 25 dB and a noise temperature of ≈ 20 K. To reject $1/f$ noise from the detectors and atmospheric fluctuations, two HEMTs are configured as a correlation receiver with an AC phase modulation. Each HEMT amplifies one of two polarizations observed through the same horn and thus the same column of atmosphere and same location on the sky at a given time. The resultant amplified signals are mixed down to 2–12 GHz, phase modulated at 1 kHz, multiplexed into three subbands, and further amplified along separate but identical intermediate-frequency (IF) amplifier chains. The signals are then multiplied together and the 1 kHz phase switch is demodulated. The resulting correlated time-averaged signal amplitude is proportional to one linear combination of the Stokes parameters (Q or U in the frame of the polarimeter) as determined by the parallactic angle of the observations and the orientation of the receiver axes. A second linear combination can be obtained after a $45°$ rotation of the polarimeter about the feed horn's optical axis, which allows one to measure both Stokes parameters and thus obtain all information about the linear polarization. Solely Stokes U (in the polarimeter reference frame) was measured in these observations. Depending on the observation strategy, the polarimeter signal will then map to some linear combination of Q and U Stokes parameters, and similarly E and B modes, on the celestial sphere.

The three subbands, in order of decreasing radio frequency, are termed J1, J2, and J3. The noise of each subband, including telescope efficiency and atmospheric absorption (but not emission) effects, was 1040, 850, and 820 ($\mu K\sqrt{s}$), respectively. Each of these subbands is demodulated with waveforms that are both in-phase and out-of-phase with the phase modulation signal. The desired signal is obtained from each in-phase demodulation (called J1I, J2I, and J3I) in addition to a null-signal noise monitor from the out-of-phase demodulation (J1O, J2O, and J3O). Further, a power splitter prior to the multiplexing stage allows a total power detection of each linear polarization termed TP0 and TP1; this signal is used for diagnostic purposes only. Additional details regarding the polarimeter can be found in Keating et al. (2003).

2.2. Telescope

The COMPASS optics were designed to be as free from systematic effects as possible. Oblique reflections of light off metallic surfaces induce spurious polarization. Scattering or diffraction by a metal or dielectric will also induce a polarized signal (Kildal et al. 1988). In any off-axis telescope there will be a systematic polarization for at least one Stokes parameter.

In conventional on-axis systems metallic or dielectric secondary supports necessarily obstruct the optical aperture and give rise to not only an overall polarization but also an increased sidelobe level. To avoid both of these effects, COMPASS uses a microwave-transparent expanded polystyrene (EPS) secondary support system. This support was designed to position and stabilize the secondary mirror to 1 mm accuracy (Farese et al. 2003).

The secondary mirror was designed to minimize aperture blockage. The 2.6 m diameter primary mirror had a 30 cm diameter hole in its center, so the secondary was constructed with a 30 cm diameter. A hole was left in the center of the secondary to prevent reillumination of the receiver. A polarized calibrator made of a thermal source and wire grid was placed behind this hole. The secondary mirror is designed to underfill the primary mirror; the primary edge illumination ends 7 cm from the edge of the primary with a much faster than Gaussian taper. This results in reducing ground pickup and spillover while still maintaining a small beam size.

In order to minimize the illumination at the edge of the secondary mirror using the existing microwave horn antenna and Dewar, it was necessary to reduce the beam size from $7°$ FWHM to $5°$ FWHM with a lens. The additional requirement that this lens be cooled to reduce its contribution to the system temperature necessitated that the lens be mounted close to the horn and thus be approximately the same diameter as the horn. A simple meniscus phase-correcting lens was selected that resulted in -15 dB secondary edge illumination. This design was based on the work by Kildal et al. (1988) and has a spherical inner surface, whose radius matches that of the radius of the horn-produced Gaussian beam, and an ellipsoidal outer surface designed to give a flat phase front at the entrance surface of the lens.

To further reduce the sensitivity of COMPASS to possible systematic effects, two levels of ground screens, one affixed to the telescope and the other stationary, were constructed. The screens mounted to the telescope were attached directly to the edge of the primary mirror. These provide an additional >50 dB of attenuation to signals from the ground, Sun, and Moon in addition to the low sidelobe level (-60 dB) of the telescope at the location of these contaminants. Observations were conducted both with and without the outer (stationary) ground screens present. Data collected with the outer ground screens present suffered from a larger scan synchronous signal (SSS) than data taken with them absent. It is believed that the combination of telescope spillover with the oblique scattering angle off the metallic surface of the ground screens induced a large polarized offset. This is discussed in more detail in § 6.

COMPASS uses a standard azimuth-elevation pointing platform. The azimuth and elevation stages are separate units. The azimuth table used was a refurbished and improved version of an existing table previously designed for use with CMB observations from the South Pole. The elevation stage was designed and built for this experiment. The position of each axis was read out by a 16 bit encoder giving a resolution of $20''$. Data acquisition of all radiometer, pointing, and "housekeeping" data (such as thermometry), as well as telescope control, was performed with a Pentium class laptop computer and 48 channel 16 bit analog-to-digital converter (ADC).

2.3. Observing Site

Our observations took place at the University of Wisconsin's Astronomy Observatory in Pine Bluff, Wisconsin ($89°.685$

TABLE 1
COMPASS POINTING

Day[a]	Observation[b]	Azimuth (arcmin)	Error (arcmin)	Elevation (arcmin)	Error (arcmin)
62............................	4	17.4	6.6	−5.4	4.2
109...........................	2	40.8	1.8	−10.2	2.4
114...........................	6	29.4	4.3	−6.0	1.8
Average[c]..............	. . .	37.8	1.6	−7.3	1.4
Uncertainty[d]........	. . .	5.3	. . .	1.8	. . .

NOTES.—Successful observations of Cas A were made on the days specified by the day number in the first column. The azimuth and elevation offsets from our target positions and the uncertainties in those offsets are given in arcminutes in the remaining columns.
[a] Day of the year 2003 in which the observation was made.
[b] The number of full, independent raster observations made at that time.
[c] The weighted average and thus the offsets used in analysis.
[d] The scatter weighted by the uncertainty of each measurement.

west longitude, $43°.078$ north latitude). The telescope was housed in a 20 m × 15 m tensioned fabric building with a wheeled, aluminum frame. This building was rolled 20 m to the south of the telescope on tracks for observations and rolled over the telescope for shelter during periods of foul weather. By moving the building rather than the telescope we were assured of the stability of the telescope and its celestial alignment.

2.4. Pointing

We initially pointed the telescope by co-aligning an optical telescope mounted on the primary mirror with the centimeter-wave beam pattern using a 31 GHz Gunn oscillator mounted on a radio tower 1.9 km west by southwest from the telescope. The source on the radio tower was quite easily visible through this optical telescope. Because of the proximity of our observing region to the NCP, several optical observations of Polaris and a number of nearby stars were made. These Polaris observations were then used to define our absolute azimuth and elevation offset and thus to define our observing region. Unfortunately, misalignment of the optical telescope resulted in an azimuth and elevation pointing error of $0°.458 \pm 0°.027$ and $-0°.107 \pm 0°.023$, respectively.

This pointing offset was discovered through observations of the supernova remnant Cas A. Cas A is circumpolar from our observing location, fairly close to our observing region, and quite bright in intensity, making it useful as a pointing tool. Three observations were made throughout the season as outlined in Table 1. There is no compelling statistically significant evidence for drifts in the pointing over the given 52 day period. Thus, a fixed pointing offset was used for all files in the analysis. Through linear fits the elevation is seen to drift at $-1'.43 \pm 2'.3$ in elevation and $10'.1 \pm 6'.9$ in azimuth per month.

2.5. Beam Determination

Raster maps of the above-mentioned "tower source" were made by using a constant-elevation raster scan. This source was essentially in the far field of the telescope, requiring only a $0'.1$ correction to the beamwidth at infinity. The FWHM obtained by fits of a Gaussian to the elevation and azimuth directions for two separate days of tower source observations are $19'.2 \pm 0'.4$ and $20'.3 \pm 0'.5$, respectively. These beam maps are confirmed by scans of Tau A. A fit of these maps with Tau A deconvolved yields a FWHM for each polarization channel and each direction (elevation and cross elevation) as provided in Table 2. Note that the analysis of the Tau A data

requires time series filtering, which may induce a larger beam size. These numbers are further confirmed by observations of Venus, which is a point source in our beam and yields beams of the two total power channels of $18'.5 \pm 1'.0$ and $19'.6 \pm 0'.8$. In our likelihood analysis we make the approximation that the beam is axially symmetric with FWHM $20'.0$, an approximation that affects our result by ≤5%.

3. CALIBRATION

Given our ~20′ beam and our sensitivity level, we require a source that is no more extended than several arcminutes and of ~10–20 Jy polarized power when averaged over our telescope's beam. Tau A (the Crab Nebula) meets these requirements and is our primary calibration source.

Historically there have been many observations of the Crab Nebula at many frequencies. If all are taken at face value, they are not in agreement with each other. To narrow the field, we have chosen to use only observations that were within our three bands of observation. These observations are corrected by the spectral index of Baars ($\alpha = -0.299 \pm 0.009$; Baars et al. 1977) and the observed decay rate ($-0.167\% \pm 0.015\%$ yr^{-1}) of Allers (Aller & Reynolds 1985) to contemporary, 30 GHz observations. Six measurements satisfy these criteria (see Table 3), resulting in a most likely total power flux measurement of 339 ± 11 Jy. These figures remained quite robust to reasonable variations in the subset of data selected and assumptions about the reported data and error bars.

Next a total of six polarized measurements are combined to obtain a most likely estimate of the polarized fraction of Tau A as $8.1\% \pm 0.9\%$ at a parallactic angle of $150° \pm 2°$. There is no observed frequency dependence of the data.

Finally, the parallactic angle, beam dilution, and atmospheric absorption of the source at the time of each observation, as

TABLE 2
COMPASS BEAM DETERMINATION

Method	Channel	Cross-Elevation (arcmin)	Elevation (arcmin)
Tau A	J1I (32–35)	21.5 ± 0.9	20.2 ± 0.9
	J2I (29–32)	22.0 ± 0.7	21.5 ± 0.9
	J3I (25–29)	23.2 ± 0.7	23.2 ± 0.9
Tower	TP0, TP1	19.2 ± 0.4	20.3 ± 0.5
Venus...................	TP0, TP1	18.5 ± 1.0	19.6 ± 0.8

NOTE.—FWHM of the beam on the sky of each subband derived from observations of Tau A, Venus, and our "tower source."

TABLE 3
COMPASS Calibration

Measurement[a]	Measured Flux[b] (Jy)	Error[b] (Jy)	Year[c]	Decay[c]	ν[d]	Correction[d]	Corrected Flux[e] (Jy)	Polarization[f]	Parallactic Angle[g] (deg)
Hobbs & Johnston (1969)	313	50	1969	0.947	31.4	1.01	300	8.1	158
Hobbs et al. (1968)...	387	72	1968	0.945	31.4	1.01	371	. . .	. . .
Kalaghan & Wulfsberg (1967)	340	53	1967	0.943	34.9	1.05	336	12	140
J. Cartwright (2003, private communication)	355	. . .	1998	0.995	31	1.01	357	7	152
Allen & Barrett (1967)..	373	. . .	1969	0.947	31.4	1.01	358	. . .	. . .
Hobbs et al. (1969)...	357	. . .	1969	0.947	31.4	1.01	343	. . .	. . .
Mayer & Hollinger (1968)	. . .	. . .	. . .	. . .	19	. . .	. . .	6.6	152
Green et al. (1975)..	. . .	. . .	. . .	. . .	15	. . .	. . .	6.4	148
Boland et al. (1966)..	. . .	. . .	. . .	. . .	14.5	. . .	. . .	8.6	146
Average	339 ± 11	. . .	. . .	. . .	. . .	. . .	. . .	8.9 ± 0.9	150 ± 2

Channel	ν[h]	Correction[h]	RJ-T[i]	Signal[j] (mK)	Signal (mV)	Gain (K V^{-1})
J1..	34	0.96	1.02	11.9 ± 3.5	3.6 ± 0.16	3.32 ± 0.98
J2..	30.5	1.00	1.02	15.3 ± 3.2	5.2 ± 0.14	2.98 ± 0.62
J3..	27.5	1.03	1.03	19.6 ± 4.0	12.4 ± 0.37	1.58 ± 0.33

Notes.—Previous measurements of Tau A near 30 GHz. The top portion of the table provides the historic measurements and the corrections needed to obtain the expected flux at the central frequency and time of COMPASS observations. The second portion shows the corrections for the individual channels, the observed signal, and the resultant gain.

[a] Reference for the described measurement. "Average" indicates the average of the expected COMPASS signal.
[b] The measured flux and uncertainty for this observation in Jy.
[c] The year of the indicated observation and the correction for source decay between then and COMPASS observations as per Aller & Reynolds (1985).
[d] The frequency of the original observation and the correction to COMPASS central frequency (30 GHz).
[e] The flux corrected for frequency and time of observation in Jy.
[f] The measured polarization percentage (if available).
[g] The measured parallactic angle of the polarization.
[h] The effective frequency and correction from the COMPASS central frequency to effective frequency of each channel.
[i] Correction from Rayleigh-Jeans to thermodynamic temperature units.
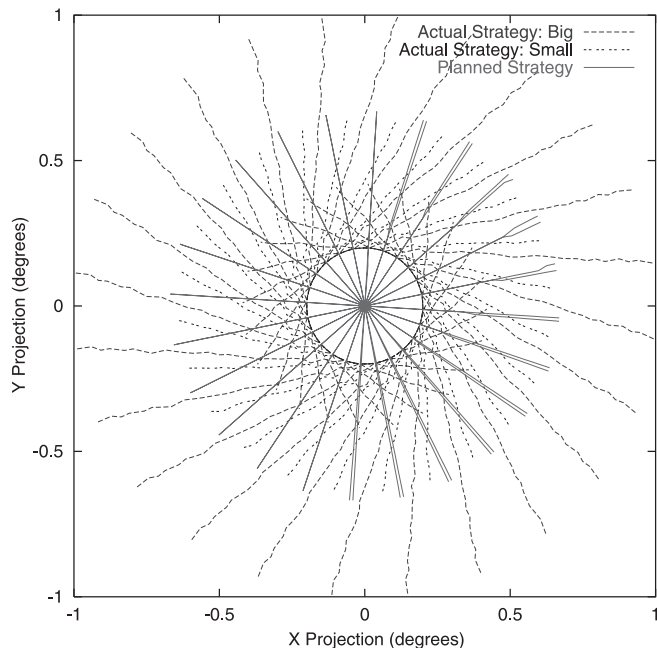[j] The best estimate for the observed signal using all listed corrections.

Fig. 1.—COMPASS scan strategy in rectangular projection about the NCP. The axes are real degrees on the sky with the positive *x*-axis corresponding to an R.A. of 0^h. It is clear how constant-elevation azimuth scans are transformed into a two-dimensional map through sky rotation. The solid line indicates our planned observations, while the dotted line shows our actual small-scan observations, and the dashed line shows the actual large-scan observations. [*See the electronic edition of the Journal for a color version of this figure.*]

well as the frequency dependence of the three correlator channels, must be taken into account. A Gaussian beam of 20$'$ (38.4 μrad^2) was used. The source is observed by performing a constant-elevation raster scan over the target region. A linear term is fitted and removed from each raster scan and the residual scans combined and compared to a template of the source derived from Hobbs & Johnston (1969) to obtain our calibration. All of these procedures are summarized in Table 3.

4. OBSERVATIONS

Our observing strategy was designed to optimize the probability of detecting a signal under current well-motivated theories while still allowing for systematics checks and tests. We attempted to observe a circular "disk" region centered on the NCP by maintaining a constant elevation and scanning the telescope in azimuth. During constant-elevation scans, the thermal load from the atmosphere remains constant and reduces both gain fluctuations of the receiver and intensity-polarization coupling in the polarimeter that could cause systematic effects. Our full scan period was varied between 10 and 20 s to reject longer term atmospheric fluctuations while maintaining stable and reliable telescope performance.

As the sky rotates, this scanned line is transformed into a cap centered on the NCP as demonstrated in Figure 1. Further, because of the sky rotation, each half sidereal day the same region of sky is observed and allows the use of difference maps as a robust test of systematic errors. Initially this "cap" was 1$°$ in diameter in order to allow deep integration on a small patch of sky to search for systematic effects. Halfway through the season this diameter was increased to 1°8 to reduce sample variance. As mentioned above, there was a small pointing offset so our actual scan strategy was not the one we intended. This resulted in a loss of symmetry and thus some

systematic tests but acceptable noise properties. Given the relative sizes of our beam, scan region, and pointing offset from the NCP, our telescope is sensitive to both *E* and *B* modes at roughly the same level. One further benefit of this scan strategy is that it simplifies the process of encoding the time stream data into a map that displays well the SSS (discussed in § 6) while still allowing for reasonable cross linking, sampling of a variety of parallactic angles, and systematics tests. A one-dimensional to two-dimensional map comparison allows simple identification of the SSS. If we plot the data in a coordinate system defined as azimuth and right ascension (R.A.), it becomes quite easy to combine the data across many days and project out the modes that correspond to the SSS (see § 6).

Finally, two configurations of the ground screens were implemented: one utilizing the two layers mentioned above and one with only the inner, comoving ground screen. These two options, combined with the two scan amplitudes mentioned above, result in a total of four "subseasons" of data termed SIGS, SOGS, BIGS, and BOGS to specify whether the small (S) or big (B) scan was used and whether the outer (O) or only inner (I) ground screens were in place. Analysis was performed on each channel in each subseason, as well as combinations of channels within a subseason, combinations of subseasons for a given channel, and all acceptable data.

5. DATA SELECTION, CLEANING, AND REDUCTION

The data analysis pipeline consists of five steps: data selection, data cleaning, intermediate azimuth map making, full map making, and power spectrum estimation. The first three steps are outlined in this section, with the last two described in greater detail in the following sections.

There were a total of 1776 hr available during our observing season, which was defined as the months of 2001 March, April, and half of May. Of these, 411 hr had sufficiently good weather to operate the experiment; 74 hr were ignored because heavy winds disrupted the azimuth pointing and control, and 28 hr were removed because of equipment failures. This leaves a total of 309 hr of usable data observing the target region. Further cuts are made, based on the data, to select periods of stable observing conditions.

The data are divided into files of 15 minutes in length. For each file six statistics are generated: three noise-based statistics (white-noise level, 1/*f* knee, and ζ [Keating et al. 2003], essentially a 1/*f* weighted sum of the power spectral density), two cross-correlations (between two correlator channels and between a correlator and total power channel), and a linear drift of the time stream. The 1/*f* knee and ζ statistics proved to be most sensitive to periods of light cloudiness or haziness. The cross-correlations were most useful in identifying more rapid contaminating events such as discrete clouds, birds, or planes interfering with the observations. Finally, the linear drift was used to identify dew formation on the foam cone.

A histogram of each statistic is formed and unions and intersections of files passing sets of cuts at the 3 σ level are made. Our results were not overly sensitive to which sets were selected. The results reported here use the two cross-correlation criteria for they retained the most data while still passing all null tests performed (see below). After all selection procedures the number of hours kept was 144, 123, and 164 for J1, J2, and J3, respectively.

Each file is then passed through a despiking procedure. Regions with excessive slopes, second derivatives, or values greater than 5 σ from the mean are flagged, cut, and filled with

white noise as estimated by the remainder of that file. Such flagged and white-noise–filled data are not included in the data analysis. This procedure removes between 0.1% and 32% of the data from any given subseason. The 32% was an anomaly; it occurred only for one channel, J3, during the first subseason where a damaged preamplifier gave rise to excessive spikes in the data intermittently. This was fixed once the cause was identified.

As a first step in the analysis, we plot the data in each 15 minute file as a function of azimuth. The sky rotation on this timescale is sufficiently small that a single bin of R.A. is needed for each file. This allows a great reduction in data size, as well as a simple treatment of our most likely systematic effect (see § 6). In order to estimate the noise in these files, a single data point is formed for each azimuth bin of each azimuth pass (i.e., leftward or rightward motion between two turnaround points in the telescope motion). The standard error of the ≈100 passes per file in each bin allows for an estimation of the noise to 10% and was in excellent agreement (<1% different) with the noise used in a full covariance estimation method.

6. MAP MAKING AND SCAN SYNCHRONOUS SIGNAL EFFECTS

One common systematic error in scanning style experiments is the presence of noncelestial signal that correlates highly with position in the scan, termed here SSS. In COMPASS such an SSS was observed and was related to a polarized offset induced by oblique reflection from the stationary ground screen or spillover to the ground. We believe that this is the result of the aggressive illumination of the secondary mirror. In all subseasons a variable offset and linear term (when plotted against azimuth) are observed and removed. In the larger scan with the stationary ground screen present a quadratic signal is detected and removed as well. Once these removals are performed, the residuals are consistent with Gaussian noise.

Detection of the SSS is performed easily by comparing maps made by binning data in only one dimension (i.e., azimuth) to those made by binning in two dimensions (i.e., azimuth and R.A.). If one has SSS contamination, the relationship between the reduced χ^2 of the one-dimensional map and that of the two-dimensional map is given by

$$\chi^2_{1D} = 1 + N_{bin}(\chi^2_{2D} - 1), \qquad (1)$$

where N_{bin} is the number of bins in the dimension that is collapsed and χ^2 refers to reduced χ^2. As shown in Table 4, there is no evidence for SSS remaining in any of the subseasons after removal of a first-order polynomial other than the big outer ground screen (BOGS) configuration.

7. MAP MAKING

As a step toward estimating the CMB polarization power spectrum, we produce a map from our data. By the term "map" here we mean a pixelized representation of the data that contains information on the spatial location, most likely data value and (nondiagonal) noise correlation matrix. The nature of polarized observations requires different mapping procedures than a simple intensity map. Traditionally, either a map of polarized intensity and orientation or a map of the Q and U Stokes parameters is provided. As COMPASS observed

TABLE 4
Scan Synchronous Signal Map Tests

Season[a]	Channel	Two-Dimensional Maps		One-Dimensional Maps	
		dof	χ^2	dof	χ^2
SIGS	J1I	244	1.00	13	0.76
	J2I	189	0.94	14	0.84
	J3I	132	1.07	13	0.73
	J1O	244	0.95	13	0.74
	J2O	189	0.95	14	0.74
	J3O	246	1.09	14	1.25
SOGS	J1I	232	1.09	13	0.45
	J2I	232	0.88	13	1.65
	J3I	240	1.00	13	1.03
	J1O	232	0.92	13	0.45
	J2O	232	1.07	13	0.84
	J3O	233	0.95	13	0.69
BIGS	J1I	182	1.08	18	0.93
	J2I	253	0.97	19	1.40
	J3I	255	0.93	19	1.20
	J1O	186	0.95	18	1.11
	J2O	180	1.24	19	1.38
	J3O	262	0.96	19	1.10
BOGS	J1I	217	1.24	19	3.96
	J2I	216	1.22	19	4.52
	J3I	212	1.17	19	4.20
	J1O	217	1.10	19	1.44
	J2O	216	1.01	19	0.68
	J3O	217	1.03	19	0.74

Notes.—The reduced χ^2 tests for azimuth and R.A.-azimuth binned maps for all subseasons and channels. Two-dimensional maps are those made in azimuth and R.A., while one-dimensional maps are made only in azimuth. Note that all are consistent with no signal except BOGS J1I, J2I, and J3I, which all show clear signs of unremoved SSS.

[a] "Season" indicates subseason: first letter is the scan size (big or small), and the second is the ground screen configuration (inner or outer ground screens).

at fixed elevation, the polarization direction information (i.e., parallactic angle) is unambiguously encoded in the R.A. and azimuth.

We initially map each (15 minute long) data file in azimuth as described above. One useful map format in which to display the data is R.A.-azimuth coordinates. This format facilitates identification of systematic effects and spurious (or real) signals. Maps of this style are provided in Figure 2. A second map format is a three-dimensional map of R.A., decl., and parallactic angle. This second map, although sparsely populated, retains the polarization information of our observations while still providing uniformly sized pixels and is used in power spectrum estimation, although it is less intuitive to display and interpret.

The noise covariance matrix is estimated from the time stream data. The off-diagonal elements of this matrix were shown to be much less than 10^{-6} of the amplitude of the on-diagonal elements and are therefore ignored. This is because the scan rate of ≈0.1 Hz is much slower than the antialiasing filter knee of 40 Hz.

Given this noise matrix and the knowledge that certain modes of the map have been filtered through our polynomial subtraction method, we next produce a generalized noise covariance matrix by adding to the noise matrix a constraint matrix as per Bond et al. (1998). The constraint matrix encodes the SSS removal process and projects the removed modes out of the map by adding noise of amplitude 10^8 times that of the
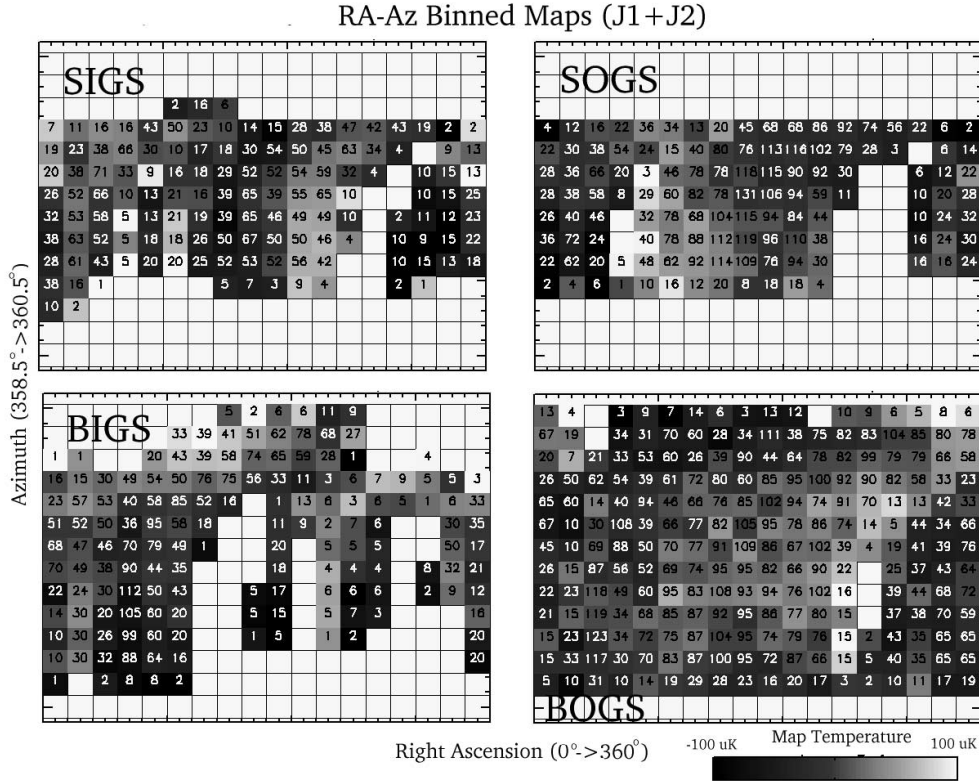
Fig. 2.—Maps plotted in R.A. and azimuth coordinates. R.A. is divided into 18 bins of $20°$ width and azimuth into 14 bins of $0°.15$ width from 358.51 to 360.46. Shown are maps for all four subseasons of the data for J1I and J2I co-added. Gray scale indicates intensity of the signal per pixel, while the number written over that pixel is the number of azimuth-binned files that contribute to the value. [*See the electronic edition of the Journal for a color version of this figure.*]

noisiest on-diagonal element (units of μK^2) to the contaminated modes. These contaminated modes are constructed for each file's azimuth map and for each order of the fit removed by forming a constraint vector and taking its outer product. These constraint templates are then multiplied by the indicated noise and added to the noise covariance matrix of each file azimuth map. These submaps are then added together in R.A.– decl.–parallactic angle space, and a resultant generalized covariance matrix, C_N, and map of the data, D, are formed as given by

$$C_{N,i} = C_{n,i} + C_{c,i},$$

$$C_N^{-1} = \sum_i^M C_{N,i}^{-1},$$

$$D = C_N \left(\sum_i^M d_i C_{N,i}^{-1} \right). \qquad (2)$$

Subtraction of a constant term from each azimuth file resulted in weakening of our result (i.e., increasing the uncertainty of the likelihood or 2 σ limit) by 25%. Removing a constant term and a slope weakened it by 50%.

8. POWER SPECTRUM ESTIMATION

Software used to estimate the power spectrum was extensively tested using simulated maps generated from a known power spectrum. These maps were provided by the University of California, Davis group and used to simulate a COMPASS time series by the University of California, Santa Barbara group.

Several hundred realizations of this data set were produced and passed through the analysis pipeline. Both the most likely value and error estimation were proved accurate and reliable for a wide range of constraint and parallactic angle situations as shown in Table 5.

A flat band power model of E-mode polarization was used to generate the theory covariance matrix, $C_T(E)$, although use of a concordance model polarization spectrum did not significantly change our results. The likelihood of the amplitude of this flat band power is calculated using the signal-to-noise ratio eigenmode method as described in Bond et al. (1998). It is worth noting that no eigenmode in our data set has an eigenvalue greater than 1. We build the total covariance matrix $C(E) = C_T(E) + C_N$ and compute the likelihood as given by

$$L(D|C(E)) = \frac{1}{(2\pi)^{N/2}} \frac{e^{-(1/2)d^T C(E)^{-1} d}}{|C(E)|^{1/2}}. \qquad (3)$$

This likelihood is calculated on a grid spaced uniformly in units of μK^2, rather than μK, to avoid overbiasing lower powers and is allowed to take values of negative power to test the correctness of the noise covariance matrix. This is performed under the requirement that the resultant covariance matrix remain positive definite; if the matrix becomes nonpositive definite for excessively negative power, that power is given a likelihood of zero.

In addition to calculating the likelihood, it is conventional to calculate the (zero lag) window function as per Bond et al. (1998). This tool is used to indicate the angular scale, or

TABLE 5
Data Analysis Pipeline Tests

Test[c]	Likelihood Probability[a]					Correct[b]	
	2.5%	16%	Most Likely	84%	97.5%	Within 68%	Within 95%
Q only	17.6	18.8	20.0	21.5	22.9	56	92
U only	16.4	17.6	19.0	20.6	22.1	68	89
$Q+U$................	14.5	16.3	18.1	20.8	23.3	63	92
$Q+10$	19.6	20.3	21.1	22.0	22.8	74	94
$Q+20$	17.5	18.0	18.5	19.0	29.5	74	99
con0.................	16.8	19.3	21.9	25.8	29.5	71	86
con1.................	14.4	16.3	18.3	21.1	23.9	63	93
con2.................	16.8	19.3	21.9	25.8	29.5	71	86
recov................	15.1	17.1	19.3	22.4	25.5	72	95

Notes.—Various test procedures applied to the likelihood estimator and full pipeline. The tests are described in detail in the footnotes below. All are made with a simulated flat band power map with an amplitude of 20.0 μK^2.

[a] The average value of the recovered band power for the indicated integrated probability.

[b] The percentage of simulations with the correct recovered power falling within the indicated confidence interval.

[c] A description of the test performed. "Q only" indicates a map of the Q-mode polarization. "U only" is a map of only U-mode polarization. "$Q+U$" is a map with each map location having both Q and U polarization values. "$Q+10$" and "$Q+20$" indicate maps with Q polarization values and values of a parallactic angle of $10°$ and $20°$, respectively. The "con" tests create sets of files of simulated azimuth-R.A. maps (our intermediate mapping) and combine them optionally adding constraints (0=none, 1=DC removed per file, 2=DC and slope removed per file). The "recov" test uses a simulated time stream generated from the simulated maps to test the full pipeline.

l-space region, to which the experiment is sensitive. As this is determined by both the telescope response pattern and observing strategy, each channel of each subseason, as well as any combination thereof, has its own window function. This is because the different scan strategies cover slightly different regions of sky and the individual channels each have their own data subsets through independent data selection. As our most significant result is obtained by combining all channels and either all subseasons or all subseasons where removal of an SSS quadratic was not required, only the window functions for these combinations are presented. Finally, as these two data combinations cover nearly identical sky (1227 pixels vs. 1228 pixels), they have essentially indistinguishable window functions. Therefore, we present in Figure 3 the COMPASS window function for the most significant result. Defining the effective l range to be that where

Fig. 3.—COMPASS window function plotted over the concordance model E-mode polarization power spectrum most favored by *WMAP*. The height of the window function has been set to the 68% confidence limit (integrated in μ K space) presented in § 9. [*See the electronic edition of the Journal for a color version of this figure.*]

the window function takes a value greater than half its maximum, we can state that COMPASS is sensitive to an l range of 93–555.

9. RESULTS

The likelihood described above is computed for each subseason, for the union of all subseasons where an SSS quadratic was not removed (a subset of the data referred to as "BEST"), and for the union of all data ("ALL"). Similarly, our analysis is performed for each frequency channel independently and for the union of all channels. Likelihood curves of the combined subseasons and channels are given in Figure 4. Five points characterizing the integrated likelihood curve (ILC) are provided in Table 6 that aid in its interpretation. These include values for the flat band power where the ILC is equal to 2.5%, 16%, 84%, and 97.5%, corresponding roughly to the conventional ± 1 and 2 σ points for the ILC of a Gaussian probability density function. Also provided is the band power at which the likelihood curve obtains its maximum. This allows for a simple comparison of the various non-Gaussian curves without requiring a series of figures.

We have also calculated the ILC for all physical values of the likelihood, namely, where the power is greater than or equal to 0. One could argue that in a case such as this with no strong detection an upper limit should be defined by finding the power at which this ILC has risen to some value. For COMPASS using the union of all data the 68%, 95%, and 98% upper limits are 348, 1036, and 1400 μK^2, respectively. We have chosen to report our result as a 95% confidence upper limit to facilitate comparison to historic CMB anisotropy upper limits (i.e., Readhead et al. 1989).

If this same procedure is performed with the ILC sampled uniformly in units of μK, one obtains limits of 12.6, 25.5, and 29.7 μK. Note that these are lower limits than those obtained by integrating the ILC when spaced uniformly in units of μK^2, demonstrating clearly the bias mentioned above. It is also worth noting that a quadratic estimator approach (as shown in the right panel of Fig. 4) performed with uniform sampling in
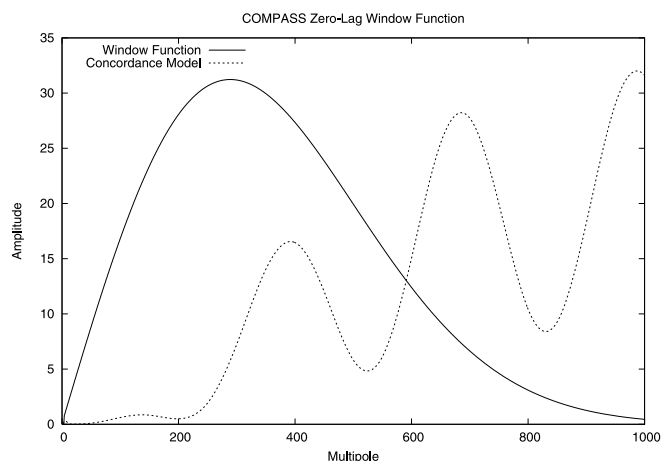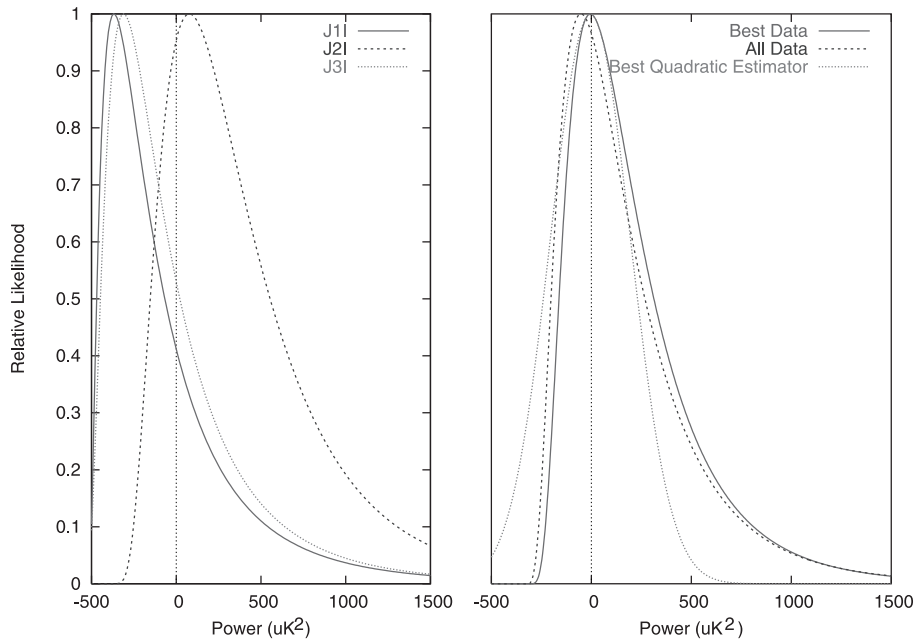
Fig. 4.—Likelihood curves in μK^2 for the E-mode flat band power for each frequency band in the "BEST" data and for all frequencies combined for the "BEST" and "ALL" data. The quadratic estimator for the "BEST" data is included as well. [*See the electronic edition of the Journal for a color version of this figure*.]

μK of this result would have given 18.5 μK as the 98% upper limit, nearly a factor of 2 lower than explicit integration of the likelihood curve spaced uniformly in μK^2. This emphasizes the need for explicit calculation of a likelihood curve because the quadratic estimator is a biased estimator in low signal-to-noise ratio situations.

In order to explore whether or not the data were contaminated by noncosmological signals, a number of difference tests were performed. These tests are referred to as jackknife tests or difference map tests, and although not necessarily optimal, they have the benefit of being both easy to implement and often easy to interpret.

Given a data vector d_i and a noise covariance matrix N_i for each of the $i = 0, 1$ maps, we can form the difference map and noise covariance

$$N_d = (N_0 + N_1), \qquad (4)$$
$$d_d = (d_0 - d_1). \qquad (5)$$

The matrices N_0, N_1 are actually the generalized noise covariance matrices and thus include information about constraints. Therefore, if a constraint is projected out of either map, it is projected out of the difference map as well. Often the convention of dividing both N_d and d_d by 2 is implemented. Had we

TABLE 6
COMPASS Results

Season[a]	Channel	2.5%	16%	Most Likely	84%	97.5%
BEST....................	J1I	−460	−380	−370	300	1290
	J2I	−180	−20	80	840	1770
	J3I	−450	−350	−310	340	1290
	J1O	−320	−160	−70	760	1790
	J2O	−280	−130	−60	840	2010
	J3O	−170	40	170	1210	2440
	ALL	−180	−72	−4	500	1128
ALL.....................	J1I	−460	−360	−340	430	1530
	J2I	−110	90	220	1130	2240
	J3I	−420	−290	−250	610	1860
	J1O	−300	−130	−20	850	1910
	J2O	−290	−130	−80	960	2370
	J3O	−160	70	200	1360	2750
	ALL	−2120	−1120	−52	476	1148

Notes.—COMPASS results grouped by subseason and channel. The values are expressed in μK^2 for the indicated values of the integrated likelihood curve. "Most Likely" is the peak location of the curve.

[a] "Season" refers to the subseason as described in Table 4, but with "BEST" indicating the union of all data represented in the subseasons with only a slope and DC removed (i.e., SIGS, SOGS, and BIGS) and "ALL" indicating all data with SSS removed as needed by channel and subseason (i.e., BEST and BOGS).

FARESE ET AL.

TABLE 7

Test Description

Cut Used	Maps Generated	Effects Tested for
Jackknife Tests		
Left-right	West-going/east-going azimuth scans	Short timescale and scan effects
First-last................	First half/last half of each subseason	Long timescale (e.g., thermal)
Subseasonal	Two subseasons	Sidelobe contamination and long timescale
Rebinning Tests		
R.A.-azimuth........	Local sidereal time and azimuth	Diurnal effects
Azimuth................	Only azimuth	Scan synchronous

Note.—This table describes briefly the different jackknife and binning tests that were performed and states what effect they are primarily attempting to discriminate.

TABLE 8

Jackknife Summary

Cut Used	Channels Implemented	Subseasons Used	Total Number
Day-night	JI, JO	All	2
Left-right	J?I, J?O	Each	24
First-last................	J?I, J?O	Each	24
Subseasonal...........	J?I, J?O	SIGS, SOGS, BIGS	18
Total	. . .	. . .	68

Notes.—Summary of the various combinations of channels and subseasons used in each jackknife test; "?" means varying over each of the three channels. For subseasonal tests only those subseasons used in the final analysis (see § 2) were used.

adopted that convention, all of our difference results would be divided by 4 for they are reported in units of μK^2.

The tests considered are explained in Table 7 and summarized in Table 8. A total of 66 of the indicated 68 tests were passed, which is consistent with there being no spurious signals in the data at the level of several tens of μK.

10. CONCLUSIONS

After one season of observations totaling approximately 150 hr of useful data, COMPASS set a 95% confidence upper limit on the polarized celestial signal of 1036 μK^2 (348 μK^2, 68% limit) in the l range 93–555. It is noteworthy that this limit is the most stringent constraint on polarized foregrounds in the NCP region on these angular scales at this frequency.

Because we are observing at a frequency where synchrotron emission is expected to be the dominant foreground, the absence of a signal at this level bodes well for future CMB polarization experiments.

REFERENCES

Allen, R. J., & Barrett, A. H. 1967, ApJ, 149, 1
Aller, H. D., & Reynolds, S. P. 1985, ApJ, 293, L73
Baars, J. W. M., Genzel, R., Pauliny-Toth, I. I. K., & Witzel, A. 1977, A&A, 61, 99
Boland, J. W., Hollinger, J. P., Mayer, C. H., & McCullough, T. P. 1966, ApJ, 144, 437
Bond, J. R., Jaffe, A. H., & Knox, L. 1998, Phys. Rev. D, 57, 2117
Farese, P. C. 2003, Ph.D. thesis, Univ. California, Santa Barbara
Farese, P. C., et al. 2003, NewA Rev., 47, 1033
Green, A. J., Baker, J. R., & Landecker, T. L. 1975, A&A, 44, 187
Hobbs, R. W., Corbett, H. H., & Santini, N. J. 1968, ApJ, 152, 43
———. 1969, ApJ, 156, L15
Hobbs, R. W., & Johnston, K. J. 1969, BAAS, 1, 244
Hu, W., & Dodelson, S. 2002, ARA&A, 40, 171
Kalaghan, P. M., & Wulfsberg, K. N. 1967, AJ, 72, 1051
Keating, B. G., O'Dell, C. W., Gundersen, J. O., Piccirillo, L., Stebor, N. C., & Timbie, P. T. 2003, ApJS, 144, 1
Kildal, P.-S., Olsen, E., & Anders, J. 1988, IEEE Trans. Ant. Prop., 36
Kogut, A., et al. 2003, ApJS, 148, 161
Kovac, J. M., Leitch, E. M., Pryke, C., Carlstrom, J. E., Halverson, N. W., & Holzapfel, W. L. 2002, Nature, 420, 772
Mayer, C. H., & Hollinger, J. P. 1968, ApJ, 151, 53
Readhead, A. C. S., Lawrence, C. R., Myers, S. T., Sargent, W. L. W., Hardebeck, H. E., & Moffet, A. T. 1989, ApJ, 346, 566